



Selective photocatalytic oxidation of benzyl alcohol into benzaldehyde with high selectivity and conversion ratio over $\text{Bi}_4\text{O}_5\text{Br}_2$ nanoflakes under blue LED irradiation

Chunxia Zheng, Guangping He, Xin Xiao*, Mingli Lu, Huan Zhong, Xiaoxi Zuo, Junmin Nan*

School of Chemistry and Environment, South China Normal University; Guangzhou Key Laboratory of Materials for Energy Conversion and Storage, Guangzhou 510006, PR China

ARTICLE INFO

Article history:

Received 15 September 2016

Received in revised form

29 November 2016

Accepted 8 December 2016

Available online 10 December 2016

Keywords:

Selective photocatalytic oxidation

Benzyl alcohol

Benzaldehyde

$\text{Bi}_4\text{O}_5\text{Br}_2$

Blue LED

ABSTRACT

Novel $\text{Bi}_4\text{O}_5\text{Br}_2$ nanoflakes with a thickness of approximately 5 nm and a band gap energy of 2.54 eV were synthesized by a rapid and energy-saving microwave route. Under blue light emitting diode (LED) irradiation and using the $\text{Bi}_4\text{O}_5\text{Br}_2$ nanoflakes as a photocatalyst, selective catalytic oxidation of benzyl alcohol (BA) into benzaldehyde (BAD) was successfully achieved with a high selectivity and conversion ratio. Compared to $\text{Bi}_{12}\text{O}_{17}\text{Cl}_2$, which has a similar blue LED light absorption capability and a band gap energy of 2.37 eV, these $\text{Bi}_4\text{O}_5\text{Br}_2$ nanoflakes exhibit superb conversion efficiency (>99%) and selectivity (>99%) toward the photocatalytic oxidation of BA into BAD. Based on the structural characterization of the as-synthesized photocatalyst, comparison of photocatalytic performances, investigation of active radicals, and quantum chemical calculations, a possible photoreaction pathway is explored and proposed. It is revealed that the high selectivity of the system comes from direct hole oxidation of alkoxide anions (BA^-) and the appropriate valence band potential (+2.41 V vs. NHE) of $\text{Bi}_4\text{O}_5\text{Br}_2$. And the high conversion ratio is attributed to the positively charged surface, large specific surface area with micro-nano structures, and effective separation of photogenerated carriers of the as-synthesized photocatalyst. In addition, the as-synthesized $\text{Bi}_4\text{O}_5\text{Br}_2$ catalyst remains stable during the photocatalytic conversion process and can be utilized repeatedly, suggesting its potential for practical applications.

© 2016 Elsevier B.V. All rights reserved.

1. Introduction

Benzaldehyde (BAD), the simplest aromatic aldehyde with an active carbonyl group, is widely used in dyestuff, perfumery, and pharmaceutical industries and is also an important organic reaction intermediate [1,2]. Besides, the selective oxidation of aromatic alcohols into corresponding aromatic aldehydes is generally identified as a fundamental reaction for direct synthesis of carbonylation compounds [3]. However, traditional synthesis of BAD through oxidation of liquid toluene or hydrolysis of benzal chloride not only forms the co-product bromobenzene since it uses sodium bromide to accelerate the reaction but also involves toxic or corrosive reagents such as chromate, hypochlorite, peroxy acids, and other chemicals [4]. And the alternative method for oxidizing benzyl

alcohol (BA) into BAD, based on metal complex compounds as the catalyst and molecular oxygen as the oxidant, also requires costly reactants such as noble metals and is a difficult way to produce BAD on a large scale [5]. Therefore, it is necessary and beneficial to develop a green, highly selective, and environmentally friendly approach to produce BAD under moderate conditions.

In past decades, semiconductor-based photocatalysis has been considered as an environmentally friendly and energy-efficient technology in the field of contamination elimination and energy conversion [6–9]. Recently, the photocatalytic partial oxidation of BA into BAD has attracted increasing attention due to its fundamental interest and potential applications. Titanium dioxide (TiO_2) was first used to convert aromatic alcohols to aldehydes under UV light, and approximately 50% conversion and 60% selectivity were achieved [10]. The low selectivity in this case can be ascribed to the fact that the hydroxyl radical formed in the UV- TiO_2 photocatalytic process is a non-selective oxidative species with strong oxidizing ability, resulting in a wide variety of reaction products. To improve

* Corresponding authors.

E-mail addresses: xiaox@scnu.edu.cn (X. Xiao), jmn@scnu.edu.cn (J. Nan).



the reaction selectivity, different types and modifications of TiO_2 , such as diverse crystal phases [11], metal ion modifications [12,13], composites [14,15], and noble-metal-loaded TiO_2 [16], have been examined. In one of the most important results, Higashimoto et al. found that BA can be adsorbed on the surface of titanium dioxide to form a special complex that becomes an active center under visible light, resulting in high selectivity and conversion from BA into BAD [17,18]. In addition to TiO_2 , CdS-based materials, such as CdS@SnO_2 nanorods [19], CdS-MOFs [20], and graphene-CdS nanocomposites [21], have also attracted attention for showing high selectivity and efficiency of BA conversion under visible light irradiation. Typically, a 60% conversion ratio and more than 80% selectivity can be gained [19]. The higher reaction selectivity over CdS under visible light than that of the UV- TiO_2 process can be attributed to the fact that there are $\cdot\text{O}_2^-$ and holes, instead of non-selective $\cdot\text{OH}^-$, acting as the main reactive species in the former.

Bismuth oxyhalides (BiOX , X=Cl, Br, and I), a type of V-VI-VII ternary semiconductor, have demonstrated outstanding photocatalytic performances owing to their unique layered structures, excellent stability, and broad tunable band gaps [22]. Recently, Zhang's group reported that BiOX materials, including $\text{Bi}_{12}\text{O}_{17}\text{Cl}_2$, $\text{Bi}_3\text{O}_4\text{Br}$, and BiOBr , can be used as visible-light-driven photocatalysts for the oxidation of BA into BAD with >99% selectivity and up to 44% conversion [23]. The authors believed that the high selectivity comes from the direct hole oxidative mechanism and appropriate band potentials of these catalysts. Very recently, Ding et al. described porous BiOCl hexagonal prisms that exhibited photocatalytic aerobic oxidation of BA to BAD with high activity and chemoselectivity under both UV and visible light [24]. According to their results, a calculated conversion of approximately 21% is obtained after visible light irradiation for 8 h. Moreover, Liu et al. reported a $\text{Bi}_{24}\text{O}_{31}\text{Cl}_{10}$ / BiOCl heterojunction photocatalyst that displayed enhanced photocatalytic activity for BA conversion with >99% selectivity and more than 40% conversion [25]. These results reveal that BiOX -based catalysts are potential candidates for the photocatalytic BA/BAD transformation.

To date, although some studies have presented good selectivity for the BA/BAD conversion, cases reporting a high conversion ratio from BA into BAD are still very limited. Lower conversion implies that additional, complicated separation processes are required to obtain pure BAD, and it may also hinder a true understanding of the photocatalytic conversion pathway of the reaction. Particular attention should be paid to developing a system that can convert BA into BAD with high selectivity as well as a high conversion ratio and to understanding its mechanism. Herein, we demonstrate a $\text{Bi}_4\text{O}_5\text{Br}_2$ nanomaterial synthesized by a facile microwave route, which could be an exceptional catalyst for photocatalytic oxidation of BA into BAD, with high selectivity (>99%) and a high conversion ratio (>99%). In particular, the reaction conditions are very mild, i.e., under blue light emitting diode (LED) illumination, at ambient temperature and pressure, without additional air/oxygen purging, and without the need for other additives. A possible conversion mechanism for the partial oxidation of BA into BAD is proposed and discussed in detail, based on the experimental results and DFT calculations.

2. Experimental

2.1. Chemicals

Bismuth nitrate pentahydrate ($\text{Bi}(\text{NO}_3)_3 \cdot 5\text{H}_2\text{O}$), potassium bromide (KBr), and acetonitrile were purchased from Tianjin Kermel Chemical Reagent Co. Ltd. Ethylene glycol (EG) was obtained from Chinasun Specialty Products Co. Ltd. Benzyl alcohol (BA) and benzaldehyde (BAD) were bought from J&K Chemical Ltd. All chemicals

were analytical grade and used as received without further purification.

2.2. Preparation of photocatalysts

In a typical synthesis of $\text{Bi}_4\text{O}_5\text{Br}_2$ nanoflakes, 1.0 mmol of $\text{Bi}(\text{NO}_3)_3 \cdot 5\text{H}_2\text{O}$ was dissolved in 50 mL EG under magnetic stirring. Next, 0.5 mmol KBr was added into the solution. After complete dissolution, the solution was transferred into a 150 mL flat-bottom flask and then heated for 4 min at 400 W under atmospheric pressure in a microwave chemical reactor (MCR-3, at a fixed frequency of 2.45 GHz, Beijing Rui Chengwei Industry Equipment Co., Ltd., China). After the reaction, the suspension was cooled down to room temperature. The resulting light yellow precipitate was collected by centrifugation and washed with deionized water and ethanol, and then dried at 60 °C in an oven. Lastly, the product was calcined at 200 °C for 2 h to obtain the final sample.

For comparison, a $\text{Bi}_{12}\text{O}_{17}\text{Cl}_2$ sample was prepared by a hydrothermal route, according to the method described by Zhang et al. [23]. And three other $\text{Bi}_4\text{O}_5\text{Br}_2$ samples were respectively synthesized using a molecular precursor hydrolysis route [26], a direct hydrolysis process [27], and a reactable ionic liquids-assisted solvothermal method [28].

2.3. Catalyst characterization

Crystal phase composition and the crystallite size of samples were analyzed by a Bruker D8 Advance X-ray diffractometer (Bruker AXS, Germany) operating with $\text{Cu K}\alpha$ radiation at a scanning speed of 6° min^{-1} . X-ray photoelectron spectroscopy (XPS, Thermo Scientific ESCALAB 250Xi, USA) measurements were used to determine the surface composition of samples. The morphology and microstructure were observed using a scanning electron microscope (SEM, JSM-6510, JEOL, Japan). UV-vis diffuse reflection spectra (DRS) was acquired on a UV-vis spectrophotometer (UV-3100, Hitachi, Japan) using BaSO_4 as a reference standard. Nitrogen adsorption-desorption isotherms and Brunauer–Emmett–Teller (BET) surface areas were analyzed using an automatic specific surface area analyzer (Micromeritics ASAP 2020, USA). Photocurrent measurements were carried out on a CHI 660C electrochemical station (Shanghai Chenhua Apparatus Corporation, China) using as-prepared samples as the working electrodes with an active area of 1.0 cm^2 , a platinum plate as the counter electrode, a commercial Ag/AgCl electrode as the reference electrode, and 0.5 mol L^{-1} Na_2SO_4 aqueous solution as the electrolyte. A 300 W xenon lamp (PLS-SXE300/300UV, Beijing Trusttech Co. Ltd., China) assembled with a UV-cut filter to remove all wavelengths lower than 420 nm was used as the light source. Electron paramagnetic resonance (EPR, JES FA-200, JEOL, Japan) was applied to detect free radicals produced in the catalytic process, using 5,5-dimethyl-1-pyrroline-N-oxide (DMPO) as a spin trap under the irradiation in three wavelength ranges ($\lambda > 420 \text{ nm}$, $> 450 \text{ nm}$, and $> 480 \text{ nm}$).

2.4. Computational methods

The frontier electron density (FED) of BA and BA^- (alkoxide anion), including the highest occupied molecular orbital (HOMO) and the lowest unoccupied molecular orbital (LUMO), were calculated using density functional theory (DFT) using the Gaussian 09 program. The optimized geometries and vibrational frequencies were obtained by the density functional B3LYP method with 6-311++G(d,p) as the basis set. All optimizations were carried out without any symmetry restrictions and were followed by harmonic frequency analyses to ensure that the optimized conformation was the true global minimum.

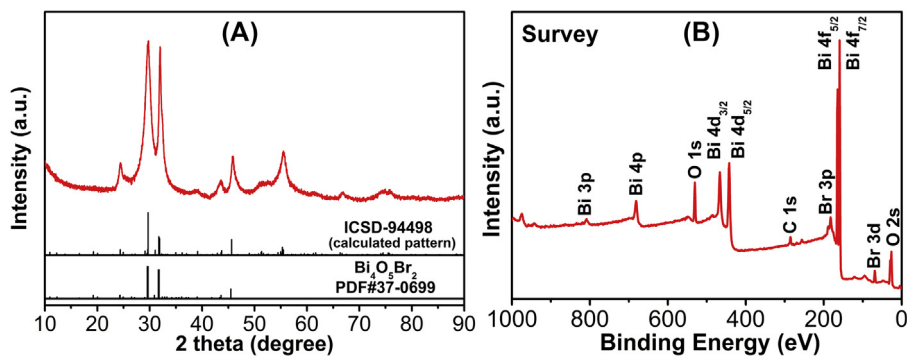


Fig. 1. (A) XRD patterns and (B) XPS survey spectrum of the as-synthesized $\text{Bi}_4\text{O}_5\text{Br}_2$.

2.5. Photocatalytic oxidation measurements

Photocatalytic selective oxidation of BA into BAD over as-prepared samples was carried out in a home-made photoreactor (Scheme S1, Supporting Information), using a 100 mL quartz beaker as the reaction vessel, surrounded with 12 W (24×0.5 W) blue LED lamps (emitting 450 ± 10 nm) as the light source, and with constant magnetic stirring. Typically, 200 mg of the sample was added to 50 mL of 0.5 mmol L^{-1} BA acetonitrile solution in a quartz beaker. Subsequently, the mixture was magnetically stirred for 1 h in the dark to ensure an adsorption-desorption equilibrium between the catalyst and BA. After the photocatalytic reaction under blue LED irradiation, the concentrations of BA and BAD were analyzed by a gas chromatograph (GC, GC 5890, Dalian Zhonghuida Scientific Instrument Co., Ltd., China) equipped with a SE-54 gas chromatograph capillary column ($30 \text{ m} \times 0.53 \text{ mm} \times 0.3 \text{ } \mu\text{m}$). The conversion of BA, yield of BAD, and selectivity of BA/BAD were defined as follows (Eqs. (1–3)):

$$\text{Conversion}(\%) = \frac{C_0 - C_{\text{BA}}}{C_0} \times 100 \quad (1)$$

$$\text{Yield}(\%) = \frac{C_{\text{BAD}}}{C_0} \times 100 \quad (2)$$

$$\text{Selectivity}(\%) = \frac{C_{\text{BAD}}}{(C_0 - C_{\text{BA}})} \times 100 \quad (3)$$

where C_0 is the initial concentration of BA, C_{BA} and C_{BAD} are the concentrations of the reaction substrate BA and corresponding BAD at a certain time after the photocatalytic reaction, respectively [29,30].

For comparison, the green LED lamps (emitting 525 ± 10 nm) experiments were also carried out using the same equipment and procedure (only replaced the lamps). And activities of samples under visible light irradiation were evaluated using a double-layer beaker photochemical reactor and a 300 W tungsten halogen lamp with a 420 nm cut off filter as light source.

3. Results and discussion

3.1. Characterization of photocatalyst

Powder X-ray diffraction (XRD) was used to determine the crystallinity and phase structure of the as-synthesized products, while X-ray photoelectron spectra (XPS) provided the quantities and chemical states of surface elements in the samples. As shown in Fig. 1A, the diffraction peaks of the as-synthesized sample match well with monoclinic $\text{Bi}_4\text{O}_5\text{Br}_2$ (JCPDS card no. 37-0699), which can be further verified by the theoretical powder diffraction pattern calculated from a crystal structure of $\text{Bi}_4\text{O}_5\text{Br}_2$ (ICSD-94498) [31]. Then its particle size was estimated to be approximately 10.6 nm according to the Debye-Scherrer formula [32]. In addition, the XPS

survey spectrum of the as-synthesized sample (Fig. 1B) confirms that it is composed of Bi, O, Br, and C elements. The presence of C is attributed to adventitious carbon species from the XPS instrument. The high-resolution XPS spectra (not shown here) further indicate that Bi, O, and Br exist as Bi^{3+} , O^{2-} , and Br^- , respectively. And the Bi/Br atomic ratio of the sample was calculated to be 2.13 on account of the areas of Bi 4f and Br 3d peaks, which agrees with the theoretical value of $\text{Bi}_4\text{O}_5\text{Br}_2$ and is consistent with the XRD analysis. According to these results, the as-synthesized sample was determined to be pure $\text{Bi}_4\text{O}_5\text{Br}_2$ with high crystallinity. In contrast, the XRD pattern of a control sample prepared according to the literature [23] is also shown in Fig. S1 (Supporting Information), clearly showing that it is a $\text{Bi}_{12}\text{O}_{17}\text{Cl}_2$ (JCPDS card no. 37-0702) sample.

The morphology and microstructure of the synthetic $\text{Bi}_4\text{O}_5\text{Br}_2$ were observed by SEM. Fig. 2 shows that the $\text{Bi}_4\text{O}_5\text{Br}_2$ sample is composed of numerous aggregated and wrinkled nanoflakes. According to the enlarged SEM image at higher magnification (inset in Fig. 2), these nanoflakes are approximately 5 nm thick and about 200–500 nm in the other two dimensions, which is in agreement with the XRD analysis. Owing to the folded structures, the nanoflakes are interspersed with each other to form three-dimensional micro-nano constructions, which can provide better contact between the catalyst and the reactants, thus may improve the reactivity.

Thus far, several methods have been reported for the preparation of nano- $\text{Bi}_4\text{O}_5\text{Br}_2$, such as the hydrothermal method [22], hydrolysis synthesis [27], reactable ionic liquid-assisted solvothermal technique [28], solvothermal-hydrolysis route [33], and structural reorganization from BiOBr [33]. However, owing to the restricted evolution of $\text{Bi}_4\text{O}_5\text{Br}_2$ under routine depositing conditions, most of these methods have to use a complex process and

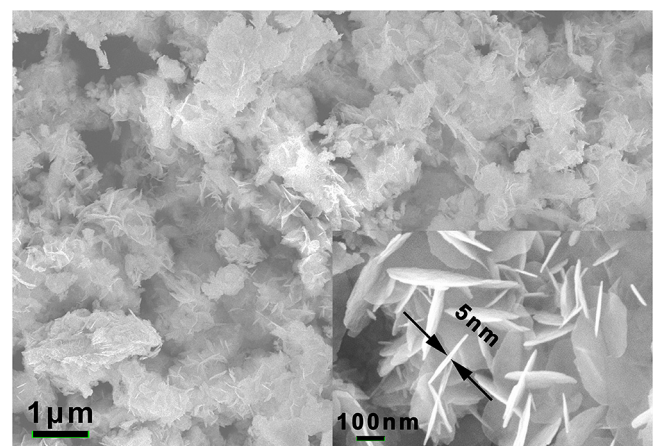


Fig. 2. SEM and high magnification SEM (inset) images of the as-synthesized sample.

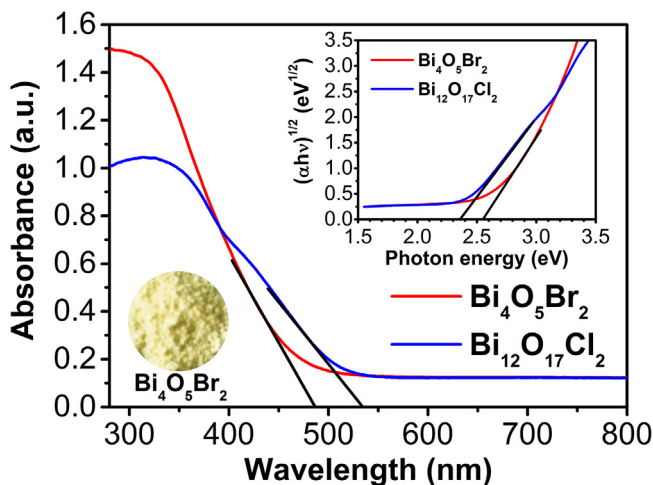


Fig. 3. UV-vis diffuse reflection spectra (DRS) for $\text{Bi}_4\text{O}_5\text{Br}_2$ and $\text{Bi}_{12}\text{O}_{17}\text{Cl}_2$; the inset displays plots of $(\alpha h\nu)^{1/2}$ vs. photon energy ($h\nu$).

reaction conditions (For example, the pH value of the system has to be carefully adjusted), receive lower crystallinity and purity, or are difficult to adapt for large-scale preparation. The intrinsic features of microwave-assisted synthesis, such as internal heating, energy saving, outstanding reduction of reaction time, and easier production of uniform and unique structures [34], have attracted increasing attention in recent years. The successful synthesis of $\text{Bi}_4\text{O}_5\text{Br}_2$ using a microwave technique and stoichiometric ratio of bismuth and bromine (2:1) without adding any additives in this work not only provides a new and effective routine to obtain ultrathin nanosized $\text{Bi}_4\text{O}_5\text{Br}_2$ with high purity, but also offers a convenient way for quick (only 4 min) and large-scale (under atmospheric pressure) preparation of this material.

UV-vis diffuse reflection spectra were used to describe the photoabsorption properties of as-synthesized $\text{Bi}_4\text{O}_5\text{Br}_2$ and $\text{Bi}_{12}\text{O}_{17}\text{Cl}_2$. Fig. 3 shows that $\text{Bi}_4\text{O}_5\text{Br}_2$ and $\text{Bi}_{12}\text{O}_{17}\text{Cl}_2$ result in different absorption edges in the spectra. The maximal absorbance wavelengths of $\text{Bi}_4\text{O}_5\text{Br}_2$ and $\text{Bi}_{12}\text{O}_{17}\text{Cl}_2$ are approximately 486 and 534 nm, respectively, indicating that both of them respond well under visible light. Then their band gap energies (E_g) can be estimated through the Kubelka-Munk function (Eq. (4)) [35]:

$$\alpha(h\nu) = A(h\nu - E_g)^n/2 \quad (4)$$

where α , h , ν , and A are the absorption coefficient, Planck constant, light frequency, and an energy-independent constant, respectively. The value of n depends on the characteristics of the semiconductor transition; for bismuth-based photocatalysts, an n equal to 4 corresponds to an indirect transition [36]. As shown in the inset of Fig. 3, the estimated E_g values of the $\text{Bi}_4\text{O}_5\text{Br}_2$ and $\text{Bi}_{12}\text{O}_{17}\text{Cl}_2$ samples are 2.54 and 2.37 eV, respectively, which is close to the reported results [23,33] and are potential photocatalysts that can work well under blue LED light ($E = 2.76 \pm 4$ eV). Then their energy band positions were further assessed by the following empirical equations (Eqs. (5–6)) [37]:

$$E_{VB} = X - E^e + 0.5 E_g \quad (5)$$

$$E_{CB} = E_{VB} - E_g \quad (6)$$

where E_{VB} and E_{CB} are the valence and conduction band edge potentials, respectively; X is the electronegativity, which is the geometric mean of the electronegativities of ingredient atoms; and E^e is the energy of free electrons on the hydrogen scale (approximately 4.5 eV). Additionally, to reflect the effect of the pH value, the E_{VB}

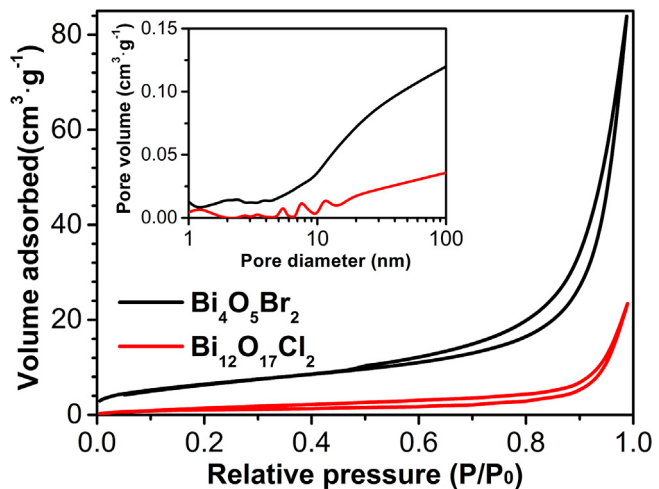


Fig. 4. Nitrogen adsorption-desorption isotherms and the corresponding pore size distribution curve (inset) for the as-synthesized $\text{Bi}_4\text{O}_5\text{Br}_2$ and $\text{Bi}_{12}\text{O}_{17}\text{Cl}_2$.

and E_{CB} potentials of the photocatalysts can be further calculated using the following equation (Eq. (7)) [38]:

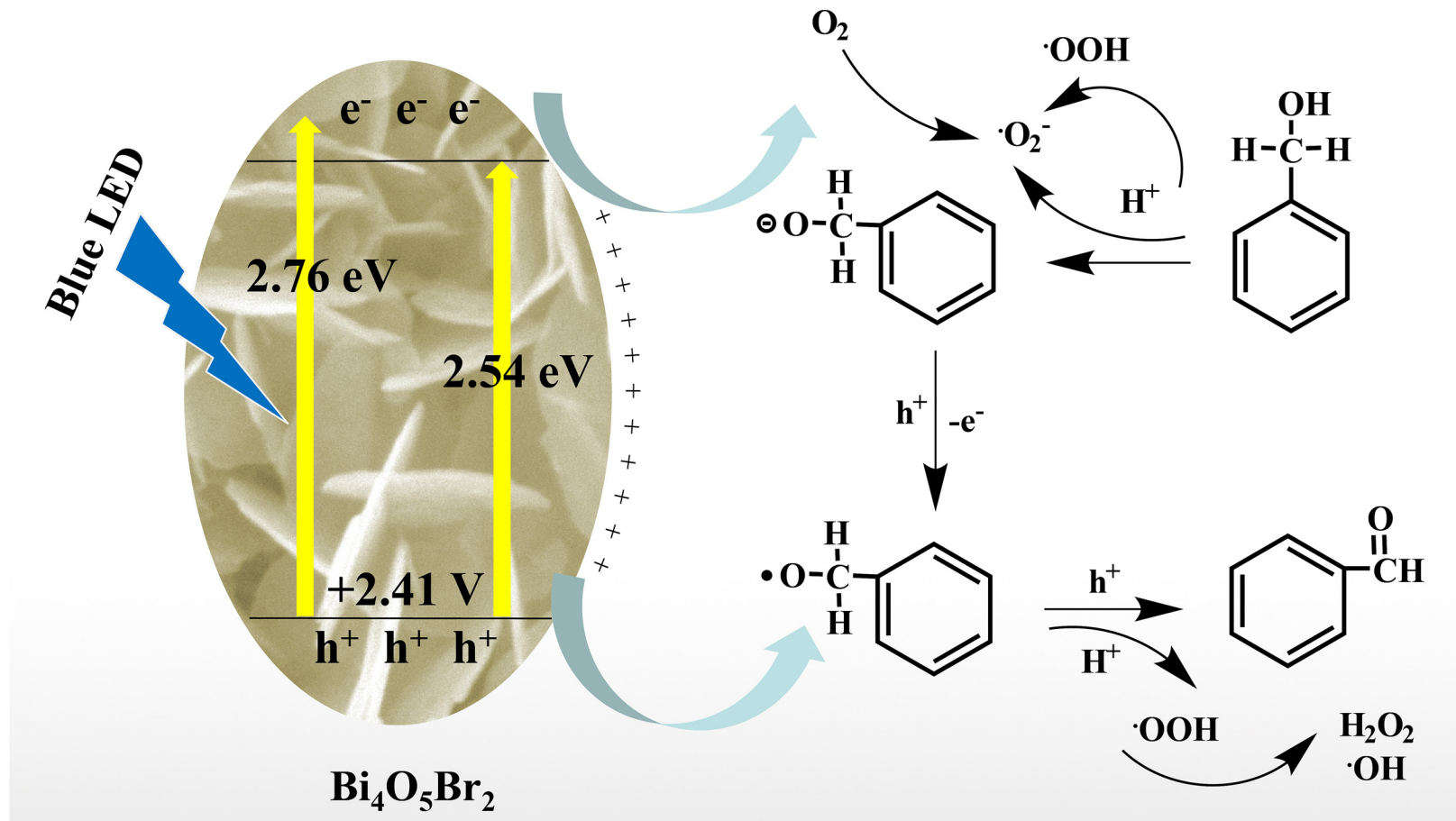
$$E = E^0 - 0.05915 \times \text{pH} \quad (7)$$

Consequently, the E_{VB} values of the as-prepared $\text{Bi}_4\text{O}_5\text{Br}_2$ and $\text{Bi}_{12}\text{O}_{17}\text{Cl}_2$ at pH = 7 are estimated to be 2.41 and 2.27 V vs. NHE, whereas their E_{CB} values are calculated to be -0.13 and -0.10 V vs. NHE, respectively. According to the above analysis and calculations, $\text{Bi}_{12}\text{O}_{17}\text{Cl}_2$ has a narrower band gap and better visible light absorption than $\text{Bi}_4\text{O}_5\text{Br}_2$, while $\text{Bi}_4\text{O}_5\text{Br}_2$ has stronger redox ability.

The BET specific surface area and porosity of the as-prepared $\text{Bi}_4\text{O}_5\text{Br}_2$ and $\text{Bi}_{12}\text{O}_{17}\text{Cl}_2$ were investigated by nitrogen adsorption-desorption isotherms. As displayed in Fig. 4, all isotherms can be identified as type IV with a H3 hysteresis loop, based on the IUPAC classification, which suggests a mesoporous structure [39]. The BET surface areas of $\text{Bi}_4\text{O}_5\text{Br}_2$ and $\text{Bi}_{12}\text{O}_{17}\text{Cl}_2$ are measured to be approximately $23.86 \text{ m}^2 \text{ g}^{-1}$ and $6.44 \text{ m}^2 \text{ g}^{-1}$, respectively, implying that the surface area of $\text{Bi}_4\text{O}_5\text{Br}_2$ is much larger than that of $\text{Bi}_{12}\text{O}_{17}\text{Cl}_2$. Their corresponding pore distributions (inset in Fig. 4) clearly reveal mesoporous features with a broad pore distribution within both samples. The larger surface area and irregular pores of $\text{Bi}_4\text{O}_5\text{Br}_2$ may be produced from the interspace and folds of nanoflakes, which is consistent with the SEM observations. Generally, a larger surface area in a catalyst can lead to the more effective adsorption of reactants and extra reactive sites during the reaction, resulting in an enhancement of reaction activity.

3.2. Photocatalytic oxidation of BA

The photocatalytic performances of the as-synthesized $\text{Bi}_4\text{O}_5\text{Br}_2$ and $\text{Bi}_{12}\text{O}_{17}\text{Cl}_2$ samples were evaluated through selective oxidation of BA into BAD under blue LED irradiation at ambient temperature and pressure. As shown in Fig. 5A, the concentration of BA decreases steadily, while the yield of its corresponding aldehyde (BAD) increases with increasing reaction time. And $\text{Bi}_4\text{O}_5\text{Br}_2$ is demonstrated superior photocatalytic activity than $\text{Bi}_{12}\text{O}_{17}\text{Cl}_2$ in identical conditions. After blue LED irradiation for 8 h, up to a 90.6% conversion ratio of BA and 99.5% selectivity can be achieved over the $\text{Bi}_4\text{O}_5\text{Br}_2$ nanoflakes, while the conversion and selectivity on $\text{Bi}_{12}\text{O}_{17}\text{Cl}_2$ are 27.9% and 95.1%, respectively. When the reaction time is further prolonged to 24 h, the former reaches 99.1% conversion efficiency and 99.4% selectivity, while the conversion of the latter increases to 34.6% and its selectivity remains approximately 95%.



Scheme 1. Proposed photoreaction mechanism for the selective photocatalytic oxidation of BA into BAD over $\text{Bi}_4\text{O}_5\text{Br}_2$ nanoflakes under blue LED irradiation. (For interpretation of the references to colour in this figure legend, the reader is referred to the web version of this article.)

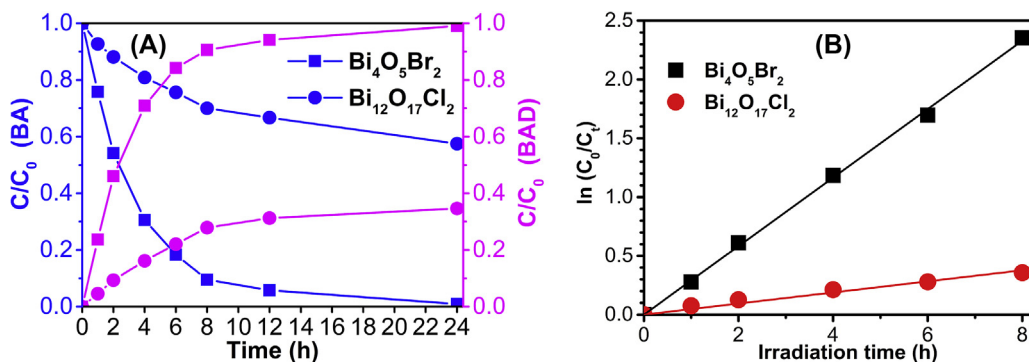


Fig. 5. (A) Photocatalytic oxidation of BA into BAD over as-synthesized $\text{Bi}_4\text{O}_5\text{Br}_2$ and $\text{Bi}_{12}\text{O}_{17}\text{Cl}_2$ samples under blue LED irradiation. (B) Linear plots of $\ln(C_0/C_t)$ versus reaction time.

Table 1

Comparison of selective photocatalytic oxidation of BA into BAD over various photocatalysts and reaction conditions reported in references.

Photocatalyst	Conversion(%)	Selectivity(%)	Light source	Extra O_2	Time(h)	Ref.
Rutile TiO_2		38.2	UV light	–	9	[10]
P25	59.5	70–85	Vis light	+	8	[23]
TiO_2	>99	>99	Blue LED	+	4	[17]
CdS	44	90	Vis light	–	8	[19]
CdS@SnO_2	78	97	Vis light	–	8	[19]
GR- CdS	65	75	Vis light	+	2	[21]
mpg- C_3N_4	57	99	Vis light	+	3	[40]
g- C_3N_4	22.1	>99	Vis light	+	8	[23]
$\text{Bi}_3\text{O}_4\text{Br}$	36.0	>99	Vis light	+	8	[23]
BiOBr	21.6	>99	Vis light	+	8	[23]
$\text{Bi}_{12}\text{O}_{17}\text{Cl}_2$	44.0	>99	Vis light	+	8	[23]
BiOCl	21	>99	Vis light	+	8	[24]
$\text{Bi}_{24}\text{O}_{31}\text{Cl}_{10}/\text{BiOCl}$	40.3	>99	Vis light	+	10	[25]
$\text{Bi}_4\text{O}_5\text{Br}_2$	90.6	>99	Blue LED	–	8	This work
$\text{Bi}_4\text{O}_5\text{Br}_2$	99.1	>99	Blue LED	–	24	This work

For further comparison, several typical results reported in the literatures are summarized in Table 1, which clearly suggests that the as-synthesized $\text{Bi}_4\text{O}_5\text{Br}_2$ nanoflakes exhibit excellent performance for the selective photocatalytic oxidation of BA into BAD, with high selectivity as well as a high conversion ratio under moderate reaction conditions.

In addition, the reaction kinetics of the selective oxidation of BA over $\text{Bi}_4\text{O}_5\text{Br}_2$ and $\text{Bi}_{12}\text{O}_{17}\text{Cl}_2$ were studied by fitting the data into the following pseudo-first-order equation (Eq. (8)) [41]:

$$-\ln\left(\frac{C_t}{C_0}\right) = k_{app}t \quad (8)$$

where C_0 and C_t are the concentrations of BA initially and at a certain time after the reaction, respectively; t is the reaction time; and k_{app} (min^{-1}) is the apparent rate constant determined by plotting $\ln(C_0/C_t)$ vs. t . As shown in Fig. 5B, the data over the two photocatalysts are well-fit to the kinetics equation, with high correlation coefficients. The k_{app} values were determined to be 0.291 and 0.047 min^{-1} for $\text{Bi}_4\text{O}_5\text{Br}_2$ and $\text{Bi}_{12}\text{O}_{17}\text{Cl}_2$, respectively. The results showed the reaction rate of BA/BAD conversion over $\text{Bi}_4\text{O}_5\text{Br}_2$ nanoflakes is more than 6 times higher than that over $\text{Bi}_{12}\text{O}_{17}\text{Cl}_2$. In order to rule out the effect of surface areas of the photocatalysts on their performances, the reaction rate constants of two samples were normalized with their surface areas. The results showed that the reaction rate of $\text{Bi}_4\text{O}_5\text{Br}_2$ ($0.0122 \text{ g min}^{-1} \text{ m}^2$) is about 1.7 times with that of $\text{Bi}_{12}\text{O}_{17}\text{Cl}_2$ ($0.00730 \text{ g min}^{-1} \text{ m}^2$), which implies that enhanced photocatalytic activity of $\text{Bi}_4\text{O}_5\text{Br}_2$ is partially attributed to its higher surface area.

For an understanding of the enhanced photocatalytic performance of $\text{Bi}_4\text{O}_5\text{Br}_2$, photoelectrochemical tests were performed to study the efficient separation of photogenerated carriers on the semiconductors. Fig. 6 shows the transient photocurrent response

(I-t curves) of the as-synthesized $\text{Bi}_4\text{O}_5\text{Br}_2$ and $\text{Bi}_{12}\text{O}_{17}\text{Cl}_2$ in several on-off cycles under visible light irradiation. Compared to $\text{Bi}_{12}\text{O}_{17}\text{Cl}_2$, the $\text{Bi}_4\text{O}_5\text{Br}_2$ nanoflakes exhibit a much stronger photocurrent (more than 3 times that of $\text{Bi}_{12}\text{O}_{17}\text{Cl}_2$), indicating the higher separation efficiency of photogenerated electrons. Therefore, taking into account the higher separation efficiency of photogenerated carriers (Fig. 6) and larger BET surface area (Fig. 4), the as-synthesized $\text{Bi}_4\text{O}_5\text{Br}_2$ exhibits a superior photocatalytic performance to $\text{Bi}_{12}\text{O}_{17}\text{Cl}_2$.

In order to study the effect of light sources on the two catalysts' performances, the photocatalytic BA/BAD conversion activity was also investigated under visible light (a tungsten halogen lamp with a 420 nm cut off filter) and green LED lamps (emitting $525 \pm 10 \text{ nm}$) irradiation. As can be seen from Fig. S2 (Supporting Information), the $\text{Bi}_4\text{O}_5\text{Br}_2$ works well under both blue LED and visible light but has a poor activity under green LED irradiation, which can be

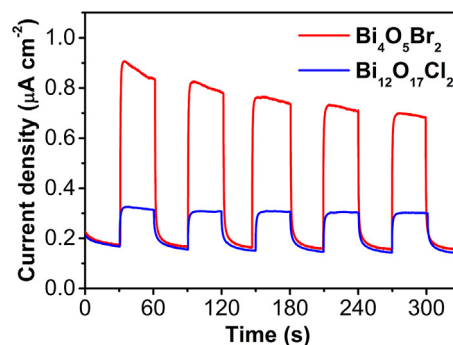


Fig. 6. Transient photocurrents of as-synthesized $\text{Bi}_4\text{O}_5\text{Br}_2$ and $\text{Bi}_{12}\text{O}_{17}\text{Cl}_2$ under visible light irradiation.

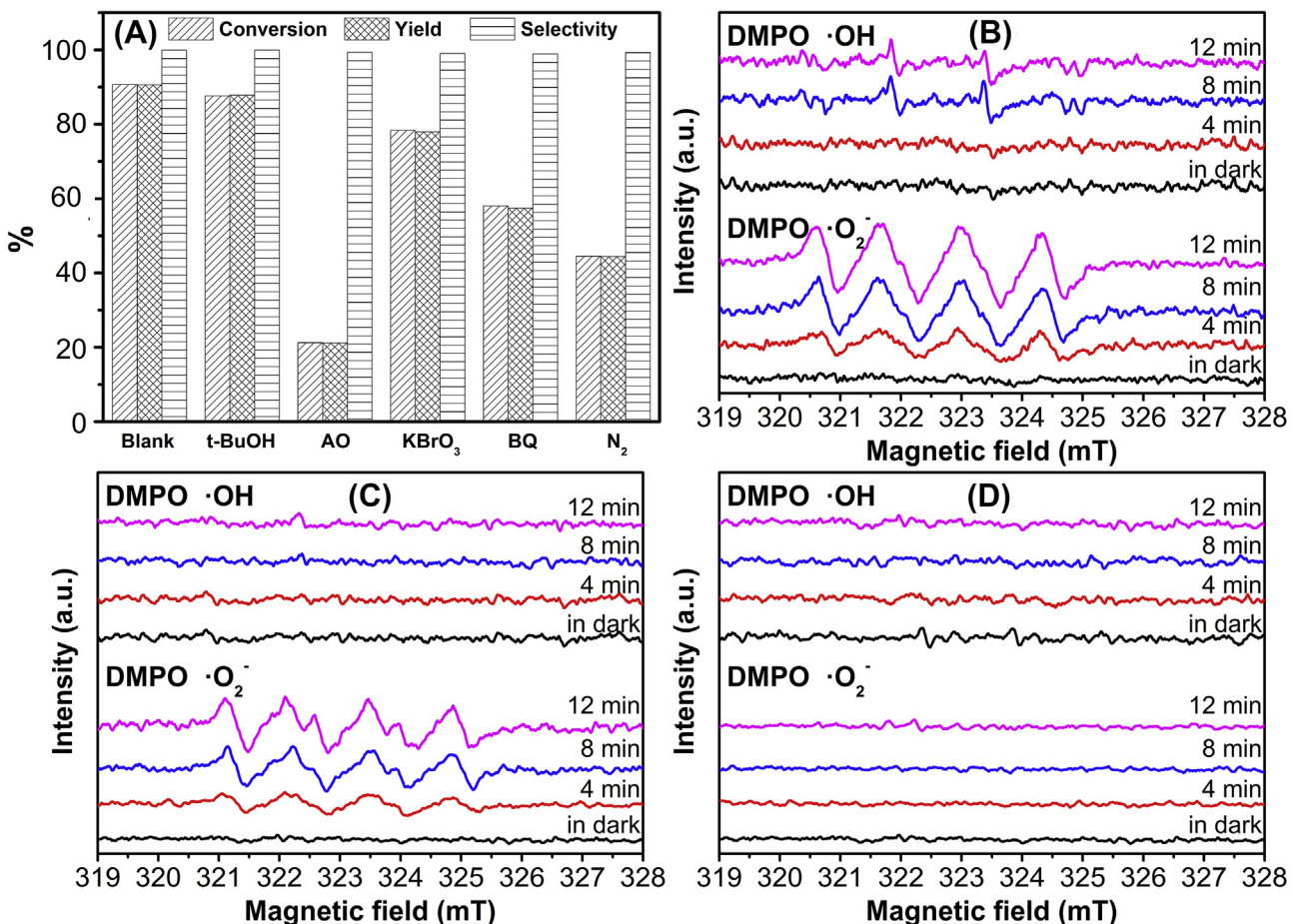


Fig. 7. (A) Control experiments of the selective photocatalytic oxidation of BA over the as-synthesized $\text{Bi}_4\text{O}_5\text{Br}_2$ nanoflakes under blue LED irradiation for 8 h in the presence of different scavengers: No scavenger (Blank), t-BuOH, AO, KBrO_3 , BQ, and N_2 ; (B-D) DMPO spin-trapping EPR spectra for DMPO-·OH and DMPO-·O₂⁻ over $\text{Bi}_4\text{O}_5\text{Br}_2$ under $\lambda > 420\text{ nm}$, $\lambda > 450\text{ nm}$, and $\lambda > 480\text{ nm}$ light irradiation.

attributed its wider band gap and weak absorption in green light. And $\text{Bi}_{12}\text{O}_{17}\text{Cl}_2$ demonstrates a rather stable performance under three different light sources may due to it has a narrower band gap. Additionally, four $\text{Bi}_4\text{O}_5\text{Br}_2$ materials synthesized from different techniques were also compared (Fig. S3, Supporting Information), displaying that all $\text{Bi}_4\text{O}_5\text{Br}_2$ samples can effectively convert BA into BAD with a high selectivity, and the microwave synthesis sample presents the best performance. The results suggest that the ability of selective conversion of BA/BAD is governed by the band structure of photocatalyst, but the microstructures and synthesis method of sample will affect its photocatalytic conversion efficiency.

3.3. Reaction mechanism

To understand the major reactive species in the selective oxidation of BA into BAD on $\text{Bi}_4\text{O}_5\text{Br}_2$ under blue LED, a series of control experiments were carried out by adding different radical scavengers to the system. In this study, tertiary butanol (t-BuOH) was introduced to extinguish $\cdot\text{OH}$, ammonium oxalate (AO) was adopted to quench h^+ , benzoquinone (BQ) was added to scavenge $\cdot\text{O}_2^-$, KBrO_3 was used for e^- trapping, and N_2 was used to remove dissolved oxygen [42–44]. As illustrated in Fig. 7A, after adding t-BuOH, the conversion of BA and selectivity to BAD remained almost the same as when no scavenger was added. However, when AO was added to quench h^+ , the conversion efficiency of BA was critically suppressed. Noticeable inhibition was also observed when KBrO_3 , BQ, and N_2 were added to the system. The results reveal that photogenerated holes and superoxide anion radicals are the

main reactive species for the photocatalytic oxidation of BA using $\text{Bi}_4\text{O}_5\text{Br}_2$ as a catalyst under blue LED irradiation, and photogenerated holes play the key role. In contrast, $\cdot\text{OH}$ radicals have a negligible effect in the photocatalytic oxidation of BA. An oxidation process based on photogenerated holes, instead of oxidation by non-selective $\cdot\text{OH}$, thus brings about the high selectivity for BA conversion [19]. The EPR technique was implemented to confirm the existence of active species. As shown in Fig. 7B–C, the characteristic peaks of DMPO-·O₂⁻ adducts distinctly developed over $\text{Bi}_4\text{O}_5\text{Br}_2$ nanoflakes after $\lambda > 420\text{ nm}$ (visible light) or $\lambda > 450\text{ nm}$ light irradiation. However, signals of DMPO-·OH adducts were hardly observed, although after a longer period of exposure, there were trace signals were detected under visible light irradiation.

It is well known that superoxide anion radicals can only be formed by reacting dissolved oxygen with photogenerated electrons when the conduction band potential of a photocatalyst is more negative than the standard redox potential of O_2/O_2^- (-0.33 V vs. NHE). In this case, the lower conduction band potential (-0.13 V vs. NHE) of $\text{Bi}_4\text{O}_5\text{Br}_2$ seems impossible to produce $\cdot\text{O}_2^-$ from a thermodynamic point of view. However, under blue LED irradiation ($E = 2.76 \pm 4\text{ eV}$), since the incident light energy is larger than its band gap energy (2.54 eV), some electrons in the valence band of $\text{Bi}_4\text{O}_5\text{Br}_2$ ($+2.41\text{ V}$ vs. NHE) can be excited to higher energy states (up to -0.39 V vs. NHE and is negative than the standard redox potential of O_2/O_2^-), and these electrons may then be trapped by O_2 to product $\cdot\text{O}_2^-$. However, when the sample is irradiated with light at $\lambda > 480\text{ nm}$, although the light is still sufficient to excite $\text{Bi}_4\text{O}_5\text{Br}_2$ (The maximal absorbance wavelengths of

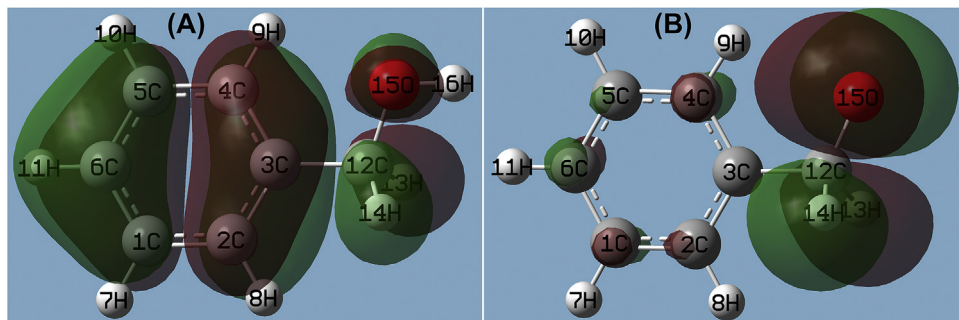


Fig. 8. Molecular structure and HOMO orbital visualization of (A) BA and (B) BA⁻ (alkoxide anion) with atoms labeled.

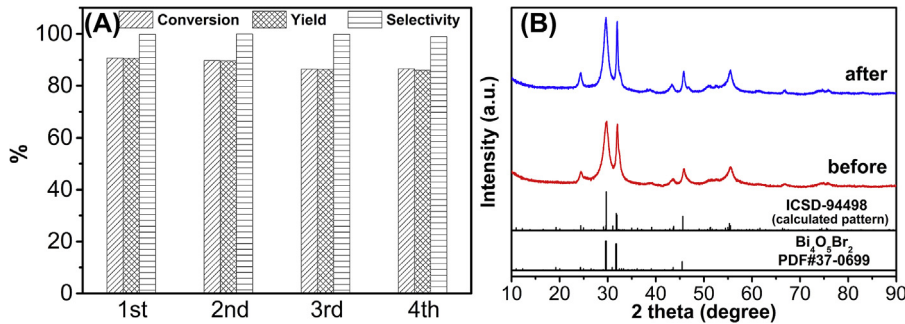
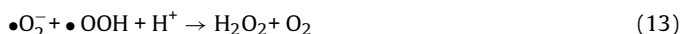
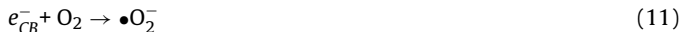
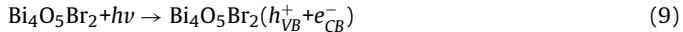


Fig. 9. (A) Recycling properties of the photocatalytic oxidation of BA into BAD over Bi₄O₅Br₂ nanoflakes under the blue LED irradiation for 8 h. (B) XRD patterns of the as-synthesized Bi₄O₅Br₂ catalyst before and after the photocatalytic reaction.

Bi₄O₅Br₂ is ~486 nm, Fig. 3), the photogenerated electrons is not satisfactory in energy to react with O₂ to form •O₂⁻. This inference can be clearly verified from EPR spectra of as-synthesized sample after different wavelengths of light irradiation (Fig. 7B–D). Thus, the mechanism of radical formation in this system can be described by the following reactions (Eqs. (9–14)):



Furthermore, since the photogenerated h⁺ plays a key role in this process and the oxidation ability of •O₂⁻ is relatively low, from the viewpoint of semiconductor photo-induced electrocatalysis [45], the valence band potential of the photocatalyst is essentially higher than the oxidation potential of BA but lower than that of BAD. In a previous study [23], the oxidation potentials of BA and BAD were electrochemically determined, showing values of 1.94 and 2.50 V vs. NHE for BA and BAD, respectively. Obviously, the valence band potentials of Bi₁₂O₁₇Cl₂ (+2.27 V vs. NHE) and Bi₄O₅Br₂ (+2.41 V vs. NHE) are suitable for photocatalytic oxidation reaction of BA into BAD. However, the latter benefits from a higher valence band potential than the former, which may bring about its stronger oxidation ability and faster reaction rate.

Recent studies [46–49] have shown that the surface oxygen vacancies (OVs) of BiOX materials can strongly affect its photocatalytic activity. By carefully analysis of the light absorption (Fig. 3), sample color (Fig. 3), high-resolution XPS spectra of Bi 4f (Fig. S4, Supporting Information), green LED activity (Fig. S2), and EPR spectra under $\lambda > 480$ nm light (Fig. 7D) of as-synthesized Bi₄O₅Br₂

sample, we consider that the role of OVs in this selective oxidation of BA into BAD system is not significant.

There are two possible reaction pathways for the oxidation of BA into BAD under aerobic conditions, including the addition of oxygen (oxygen-containing species) followed by dehydration and the continuous loss of two hydrogen atoms in BA. The scavenging experiments (Fig. 7) prove that •OH can be ignored in this system. And through applying the ¹⁸O isotope labeling technique, Zhang et al. confirmed that molecular oxygen and its derivatives are not directly involved in the construction of BAD over BiOX catalysts under visible light [23]. Hence, the key step in this system is dehydrogenation based on direct oxidation by photogenerated holes. However, since the BA must lose two hydrogen atoms in order to form BAD on account of its chemical composition and there are three different types of hydrogen atoms in molecular BA, namely, O-H, C-H, and Ph-H [50], the reason why BA loses two distinct H (one O-H and one C-H) to give BAD remains unclear.

To solve this problem, quantum chemical calculation of molecular BA was performed, as shown in Fig. 8A and Table 2. According to the frontier electron density (FED) theory, the first attack for a radical-based reaction will happen at the position of the highest density of the sum of HOMO and LUMO energies [51], while the location of the first reaction for direct hole oxidation is predicted on the basis of 2FED²_{HOMO} [52]. In the results for BA, the highest 2FED²_{HOMO} values are found at the C₃ and C₆ atoms (Table 2), implying that the electrons in these positions will be the first to be extracted by holes (h⁺). Obviously, this deduction is unreasonable since these steps will lead to the loss of H on the benzene ring (Ph-H) and may result in ring breakdown. On the other hand, since alcohols are a type of weak acid which can be deprotonated to yield benzyloxides (alkoxide anions), calculation for BA⁻ was also conducted using the same method. As shown in Fig. 8B and Table 2, the results are completely different when compared with BA. From the results, electrons on the O₁₅ and C₁₂ atoms in BA⁻ are more easily captured by holes, resulting in a reconstruction and dehydrogenation (C-H) process. The differences between BA and BA⁻ can be

Table 2Calculation results of frontier electron densities of BA and BA⁻.

Atom	BA		BA ⁻	
	2FED ² _{HOMO}	FED ² _{HOMO} + FED ² _{LUMO}	2FED ² _{HOMO}	FED ² _{HOMO} + FED ² _{LUMO}
C1	0.049	0.184	0.013	13.163
C2	0.092	4.156	0.005	7.463
C3	0.250	5.503	0.046	42.839
C4	0.168	1.102	0.027	8.632
C5	0.093	0.194	0.006	2.909
C6	0.246	0.353	0.010	46.332
C12	0.028	19.841	0.172	48.151
O15	0.045	0.117	0.729	0.375

clearly observed by the visualization of electron density, as shown in Fig. 8. Since the photogenerated holes act as electron acceptors (lacking in electrons), they tend to snatch electrons to form a stable structure. Undoubtedly, those atoms in the molecule that occupy a higher electron density would be more easily lost. Thus, the pathway based on BA⁻ dehydrogenation appears to be more credible than that of BA, according to the theoretical calculations.

Then why do the photogenerated holes prefer to react with BA⁻ instead of BA even though the latter has a much higher concentration than the former in neutral condition? Zeta potential measurements on a Bi₄O₅Br₂ suspension were carried out to determine the surface charge on the catalyst. As shown in Fig. S5 (Supporting Information), the surface charge on Bi₄O₅Br₂ is positive in the neutral state, over test three times. Thus, the photocatalyst is likely to adsorb anions in the system on its surface, implying that photogenerated holes could more effectively interact with BA⁻.

Combining the above results and analysis, a possible reaction pathway of selective photocatalytic oxidation of BA into BAD over Bi₄O₅Br₂ nanoflakes under blue LED light is proposed in Scheme 1. First, BA undergoes an ionization equilibrium to produce BA⁻ and H⁺. These alkoxide anions are adsorbed on the surface of Bi₄O₅Br₂ nanoflakes due to its positive charge surface. Upon being exposed by blue LED, the valence band electrons of Bi₄O₅Br₂ are excited into its conduction band to form photogenerated carriers. Electrons in the conduction band of the photocatalyst can be captured by dissolved O₂ to form \bullet O₂⁻. This species can further interact with H⁺ to produce other hydroxide-containing derivatives, leaving photogenerated holes on the surface of Bi₄O₅Br₂. Then, BA⁻ reacts with photogenerated holes and releases an electron to form carbon radicals. These carbon radicals are less stable and tend to react with holes to lose another electron, and are subsequently reconstructed and take place dehydrogenation step to produce BAD. Thus, the complex process of the oxidation of BA to BAD was simplified in a one-step procedure, in which BA⁻ reacts with photogenerated holes on the Bi₄O₅Br₂ surface to reduce a hydrogen on its hydroxymethyl group, resulting in the high selectivity for BA/BAD. At the same time, the photogenerated electrons react with dissolved O₂ (act as electrons scavenger) and H⁺, which further aids the progress of the reaction by consuming the H⁺ ionized from BA. Since Bi₄O₅Br₂ exhibits a positive charge surface, it can effectively adsorb BA⁻ and release BAD from its surface after the reaction, thus resulting in a high conversion efficiency. By coupling the large specific surface area and high separation efficiency of photogenerated carriers of the as-synthesized Bi₄O₅Br₂ photocatalyst, a high conversion and high selectivity to the BA/BAD transformation is ultimately achieved.

3.4. Reusability and stability

To examine the recyclability of the as-synthesized Bi₄O₅Br₂ nanoflakes, the used photocatalyst was collected by centrifugation, washed with deionized water and ethanol, dried at 60 °C, and reused three times under identical conditions. As shown in Fig. 9A,

the Bi₄O₅Br₂ sample shows high stability and retains a good photocatalytic performance during the four reaction cycles. Additionally, the XRD analysis of the Bi₄O₅Br₂ catalyst before and after the photocatalytic reaction reveals that its structure remained unchanged (Fig. 9B). Therefore, the as-synthesized Bi₄O₅Br₂ nanoflakes are stable and could be potentially used for practical industrial applications.

4. Conclusion

In summary, a novel Bi₄O₅Br₂ nanoflakes photocatalyst was successfully synthesized through a simple, fast, and energy-saving microwave route. The as-synthesized photocatalyst presents excellent photocatalytic oxidation efficiency and selectivity toward the conversion of BA into BAD under blue LED irradiation. The high selectivity and conversion ratio is related to the direct hole oxidative mechanism and the features of synthetic catalysts, including a suitable band gap energy and valence band position, positive charge surface, nanoflakes-based micro-nano structures, large specific surface area, and effective separation of photogenerated carriers. Moreover, the as-prepared catalyst exhibits high stability, suggesting its potential for practical applications.

Acknowledgements

This work was financially supported by the National Natural Science Foundation of China (No. 21477040) and the Natural Science Foundation of Guangdong Province (Nos. 2015A030313393, S2012040007074).

Appendix A. Supplementary data

Supplementary data associated with this article can be found, in the online version, at <http://dx.doi.org/10.1016/j.apcatb.2016.12.026>.

References

- [1] G.D. Yadav, C.K. Mistry, *J. Mol. Catal. A: Chem.* 172 (2001) 135–149.
- [2] M.M. Baizer, *J. Appl. Electrochem.* 10 (1980) 285–290.
- [3] G.L. Zhuo, X.Z. Jiang, *Catal. Lett.* 87 (2003) 225–227.
- [4] V.R. Choudhary, P.A. Chaudhari, V.S. Narkhede, *Catal. Commun.* 4 (2003) 171–175.
- [5] T. Mallat, A. Baiker, *Chem. Rev.* 104 (2004) 3037–3058.
- [6] A. Fujishima, *Nature* 238 (1972) 37–38.
- [7] J. Yu, J. Low, W. Xiao, P. Zhou, M. Jaroniec, *J. Am. Chem. Soc.* 136 (2014) 8839–8842.
- [8] X. Chen, S. Shen, L. Guo, S.S. Mao, *Chem. Rev.* 110 (2010) 6503–6570.
- [9] C.S. Turchi, D.F. Ollis, *J. Catal.* 122 (1990) 178–192.
- [10] S. Yurdakal, G. Palmisano, V. Loddo, V. Augugliaro, L. Palmisano, *J. Am. Chem. Soc.* 130 (2008) 1568–1569.
- [11] C.J. Li, G.R. Xu, B.H. Zhang, J.R. Gong, *Appl. Catal. B: Environ.* 115 (2012) 201–208.
- [12] D. Spasiano, L. Rodriguez, J.C. Olleros, S. Malato, R. Marotta, R. Andreozzi, *Appl. Catal. B: Environ.* 136 (2013) 56–63.
- [13] S. Higashimoto, R. Shirai, Y. Osano, M. Azuma, H. Ohue, Y. Sakata, H. Kobayashi, *J. Catal.* 311 (2014) 137–143.

[14] M.Q. Yang, N. Zhang, Y.J. Xu, *ACS Appl. Mater. Interfaces* 5 (2013) 1156–1164.

[15] J.C. Colmenares, W.Y. Ouyang, M. Ojeda, E. Kuna, O. Chernyayeva, D. Lisoviytskiy, S. De, R. Luque, A.M. Balu, *Appl. Catal. B: Environ.* 183 (2016) 107–112.

[16] W. Feng, G.J. Wu, L.D. Li, N.J. Guan, *Green Chem.* 13 (2011) 3265–3272.

[17] S. Higashimoto, N. Kitao, N. Yoshida, T. Sakura, M. Azuma, H. Ohue, Y. Sakata, *J. Catal.* 266 (2009) 279–285.

[18] H. Kobayashi, S. Higashimoto, *Appl. Catal. B: Environ.* 170 (2015) 135–143.

[19] Y. Liu, P. Zhang, B.Z. Tian, J.L. Zhang, *ACS Appl. Mater. Interfaces* 7 (2015) 13849–13858.

[20] F. Ke, L.H. Wang, J.F. Zhu, *Nano Res.* 8 (2015) 1834–1846.

[21] Z.Y. Ren, J.Y. Zhang, F.X. Xiao, G.C. Xiao, *J. Mater. Chem. A* 2 (2014) 5330–5339.

[22] X. Xiao, C. Liu, R. Hu, X. Zuo, J. Nan, L. Li, L. Wang, *J. Mater. Chem.* 22 (2012) 22840–22843.

[23] X. Xiao, J. Jiang, L. Zhang, *Appl. Catal. B: Environ.* 142–143 (2013) 487–493.

[24] L.Y. Ding, H. Chen, Q.Q. Wang, T.F. Zhou, Q.Q. Jiang, Y.H. Yuan, J.L. Li, J.C. Hu, *Chem. Commun.* 52 (2016) 994–997.

[25] X.Y. Liu, Y.G. Su, Q.H. Zhao, C.F. Du, Z.L. Liu, *Sci. Rep.* 6 (2016) 28689.

[26] Y. Bai, T. Chen, P. Wang, L. Wang, L. Ye, *Chem. Eng. J.* 304 (2016) 454–460.

[27] M. Li, Y.J. Cui, Y.S. Jin, H. Li, *RSC Adv.* 6 (2016) 47545–47551.

[28] J. Di, J.X. Xia, M.X. Ji, S. Yin, H.P. Li, H. Xu, Q. Zhang, H.M. Li, *J. Mater. Chem. A* 3 (2015) 15108–15118.

[29] S. Meng, X. Ye, X. Ning, M. Xie, X. Fu, S. Chen, *Appl. Catal. B: Environ.* 182 (2016) 356–368.

[30] X. Dai, M. Xie, S. Meng, X. Fu, S. Chen, *Appl. Catal. B: Environ.* 158 (2014) 382–390.

[31] E. Keller, V. Kramer, M. Schmidt, H. Oppermann, *Invest. New Drug* 217 (2002) 845–857.

[32] X. Xiao, R. Hao, X. Zuo, J. Nan, L. Li, W. Zhang, *Chem. Eng. J.* 209 (2012) 293–300.

[33] L.Q. Ye, X.L. Jin, C. Liu, C.H. Ding, H.Q. Xie, K.H. Chu, P.K. Wong, *Appl. Catal. B: Environ.* 187 (2016) 281–290.

[34] G. Qiu, S. Dharmarathna, H. Genuino, Y. Zhang, H. Huang, S.L. Suib, *ACS Catal.* 1 (2011) 1702–1709.

[35] X. Zhang, Z.H. Ai, F.L. Jia, L.Z. Zhang, *J. Phys. Chem. C* 112 (2008) 747–753.

[36] F. Qin, G. Li, R. Wang, J. Wu, H. Sun, R. Chen, *Chem. Eur. J.* 18 (2012) 16491–16497.

[37] Y. Xu, M.A.A. Schoonen, *Am. Mineral.* 85 (2000) 543–556.

[38] J. Cao, B. Xu, H. Lin, B. Luo, S. Chen, *Dalton Trans.* 41 (2012) 11482–11490.

[39] K. Sing, D.H. Everett, R. Haul, L. Moscou, R.A. Pierotti, J. Rouquerol, T. Siemieniewska, *Pure Appl. Chem.* 57 (1985) 603–619.

[40] F. Su, S.C. Mathew, G. Lipner, X. Fu, M. Antonietti, S. Blechert, X. Wang, *J. Am. Chem. Soc.* 132 (2010) 16299–16301.

[41] J. Xu, W. Meng, Y. Zhang, L. Li, C. Guo, *Appl. Catal. B: Environ.* 107 (2011) 355–362.

[42] N. Qin, Y. Liu, W. Wu, L. Shen, X. Chen, Z. Li, L. Wu, *Langmuir* 31 (2015) 1203–1209.

[43] Y. Huang, H. Li, M. Balogun, W. Liu, Y. Tong, X. Lu, H. Ji, *ACS Appl. Mater. Interfaces* 6 (2014) 22920–22927.

[44] Y. Zhang, N. Zhang, Z. Tang, Y. Xu, *ACS Nano* 6 (2012) 9777–9789.

[45] X. Xiao, S. Tu, M. Lu, H. Zhong, C. Zheng, X. Zuo, J. Nan, *Appl. Catal. B: Environ.* 198 (2016) 124–132.

[46] J. Li, G. Zhan, Y. Yu, L. Zhang, *Nature Commun.* 7 (2016) 11480.

[47] H. Li, J. Shang, Z. Ai, L. Zhang, *J. Am. Chem. Soc.* 137 (2015) 6393–6399.

[48] K. Zhao, L. Zhang, J. Wang, Q. Li, W. He, J.J. Yin, *J. Am. Chem. Soc.* 135 (2013) 15750–15753.

[49] H. Li, J. Shi, K. Zhao, L. Zhang, *Nanoscale* 6 (2014) 14168–14173.

[50] L. Zhao, B. Zhang, X. Xiao, F.L. Gu, R. Zhang, *J. Mol. Catal. A: Chem.* 420 (2016) 82–87.

[51] N. San, A. Hatipoğlu, G. Koçtürk, Z. Çınar, *J. Photochem. Photobiol. A: Chem.* 146 (2002) 189–197.

[52] K. Fukui, T. Yonezawa, H. Shingu, *J. Chem. Phys.* 20 (1952) 722–725.